Chapter 3

Low-Noise Airfoil and Wind Turbine Design

Wei Jun Zhu, Wen Zhong Shen and
Jens Nørkær Sørensen

Additional information is available at the end of the chapter

http://dx.doi.org/10.5772/63335

Abstract

This chapter describes design and optimization of low-noise airfoil and wind turbines. The airfoils and wind turbine blades are designed with the objective of high-power performance. The aerodynamic noise is one of the important constraints for the optimization. The power coefficient of an airfoil is computed with the blade element momentum theory. The solution of the power coefficient is assumed to be maximized when the axial induction factor is 1/3. The airfoil noise is simulated with a semi-empirical model that requires airfoil boundary layer parameter as input. The airfoil and blade design process can be integrated such that the blade is designed with the desired airfoils. The results of three airfoil families and two rotor blades are presented, which are designed with the requirements of high-power performance and low-noise generation.

Keywords: cost of energy, design and optimization, low-noise wind turbine, wind turbine aeroacoustics, wind turbine aerodynamics

1. Introduction

Wind energy is one of the most attractive energy sources compared with the coal-based energy sources. In addition to the energy shortage, CO_2 emission is the worldwide concern of using conventional energy sources. Other types of air pollutants such as SO_x, NO_x and dust are becoming significant problems for some cities at densely populated areas. Also, as the size of wind turbine is getting larger, rotor noise has become a barrier for future development. For using wind energy, one of the major objectives in wind turbine airfoil design is to achieve a high aerodynamic performance that ensures wind turbine blade to operate with high-power performance. When it comes to social acceptance, the noise aspect becomes very important in

particular for onshore turbines, such that low-noise wind turbine design is an important competitive parameter. Therefore, the overall objective behind the design work is to make wind energy production more efficient, while at the same time lowering noise emission through gaining fundamental insight into the airfoil noise generation mechanisms.

The wind turbine noise regulation is restricted in Europe because it is more densely populated than many other countries outside EU. In Denmark, the noise limits for wind turbine in open area is 44 dB at a wind speed of 8 m/s and 42 dB at a wind speed of 6 m/s [1]. In addition, there is a low frequency limit (<20 dB) applied for wind turbine noise received inside a nearby house. Previous works on wind turbine airfoil design were aimed at high lift and high lift to drag ratio, such as the Wortmann FX 77-W-series airfoils [2] and the NREL airfoils [3, 4]. Later on, Björk [5, 6], Timmer and Van Rooij [7], Dahl and Fuglsang [8], and Fuglsang and Bak [9] made some significant contributions in designing wind turbine airfoils, and the designed airfoils were named with the institution's names (FFA, DU, and RISØ airfoils). Since 1990s, many researchers at Technical University of Denmark (DTU) have made advance research in designing wind turbine airfoils [8–12]. As the most important design objective, these wind turbine airfoils meet the demand of high lift to drag ratio and some of them are designed for low-noise emission [12].

To begin with airfoil and blade design, a profile shape can be described by the Joukowski transformation such that an airfoil shape can be represented by a series of trigonometric functions. Using this method, the DTU-LN1xx airfoils are designed [12]. Based on these airfoils, the LN2xx and LN3xx airfoil families are further developed. These airfoils are generated with a shape perturbation function that uses the LN1xx airfoils as baseline airfoils. All of these airfoils are noise constrained with a semi-empirical noise prediction model [13, 14]. To develop high-performance wind turbine blade, it is desired to have the airfoils designed for a specific blade. The above-mentioned LN2xx and LN3xx airfoils are designed for a 3 MW wind turbine and a 20 MW wind turbine, respectively. In the optimization process, the airfoils and blade design is integrated. The advantage is that the flow geometry over each rotor cross-section is optimized. A 2D blade element momentum (BEM) model is introduced during the optimization loop, which iteratively computes the local maximum C_p at each rotor cross-section.

This chapter is organized as follows: Section 2 introduces the 2D airfoil design method; Section 3 presents the airfoil and blade integrated design method; Section 4 presents results from aerodynamic and aeroacoustic simulations; and Section 5 concludes the work.

2. The 2D airfoil designs

In this section, the related design about the 2D airfoils is described. The Reynolds number, Mach number, angle of attack and surface roughness are flow-related parameters that need to be considered while applying the flow solver. The design objectives, constraints and some results are provided.

http://dx.doi.org/10.5772/63335

2.1. The flow conditions

The LN1xx, LN2xx and LN3xx airfoils are designed at Reynolds number around 1.6×10^6, 3×10^6 and 16×10^6, respectively, depending on the airfoil chord and radial location. According to the local flow at each blade section, the Mach number at each blade section also varies. To consider different flow conditions, the design angle of attack is between 3° and 10°. Numerical computations go through each angle of attack with a step of 1°. Such a wide range of angle of attack also takes into account the off-design condition. To model the airfoil roughness condition, the free transition simulation is based on the e^n model, where $n = 9$; the forced transition simulation is performed by giving the upper and lower transition points at 5% and 10% chords position, measured from the leading edge. The numerical tool Xfoil developed by Drela [15] is applied for airfoil boundary layer calculations. The code is used iteratively inside the optimization. The flow conditions, such as Reynolds number, angle of attack, Mach number and transition condition are written in an input script that is recognized by the Xfoil code.

2.2. The design variables

Although a number of functions can be used to describe airfoil shapes, however, it is imperative to choose proper functions to represent airfoil geometry. Ideally, an airfoil profile can be transformed into a near circle by the Joukowski transformation:

$$\varsigma = z + a^2 / z \tag{1}$$

where a = chord/4, ς and z are the complex variables in the airfoil plane and the near circle plane, respectively. The coordinate of z can be described as

$$z = a\exp\left(\varphi + \mathrm{i}\theta\right) \tag{2}$$

where ϕ is a function of θ. Using the concept of the Taylor series expansion, the function ϕ is expressed as [11]

$$\varphi(\theta) = \sum_{n}^{k=1}\left(a_k\left(1-\cos(\theta)\right)^k + b_k\sin^k(\theta)\right)\varphi(\theta) \tag{3}$$

where a_k and b_k are the design variables that determine airfoil shapes. By combining Eqs. (1), (2) and (3), an airfoil shape is represented by a series of trigonometric functions. Such a function is used for the design of LN1xx airfoils.

For the design of LN2xx and LN3xx airfoils, instead of creating a new airfoil shape from beginning, a shape perturbation function is applied to modify an existing airfoil. The idea of using such a function is to save computational time and inherit the shape from the previous airfoils that already have good performance. The shape perturbation function used for the upper surface is

$$\Delta y_{\mathrm{u,l}}(i) = \sum_{N}^{k=1} f_{\mathrm{u,l}}(k) P_{\mathrm{u,l}}(k,i) \tag{4}$$

where the subscripts u and l indicate upper and lower airfoil surfaces, respectively, i is the index of the x and y coordinates, and k is the index of the shape modes. The shape functions for each mode along the x-coordinate are

$$P_{\mathrm{u,l}}(k.i) = \sin^{\xi_{\mathrm{u,l}}}\left(\pi x_{\mathrm{u,l}}(i)^{g(k)}\right) \tag{5}$$

The amplitudes $f_{\mathrm{u,l}}$ are the design variables, and with the power factors $\xi_{\mathrm{u,l}}$ a total number of design points is dofs = 2*N + 2. g is a given vector which is the exponent of x. For example, the choice of g could be g = [0.1 0.2 0.3 0.5 1 3 5 8]. Because $x_{\mathrm{u,l}} \in [0, 1]$, Eq. (4) provides zero value at leading edge and trailing edge points. Therefore, the leading edge and the trailing edge are naturally fixed without being perturbed.

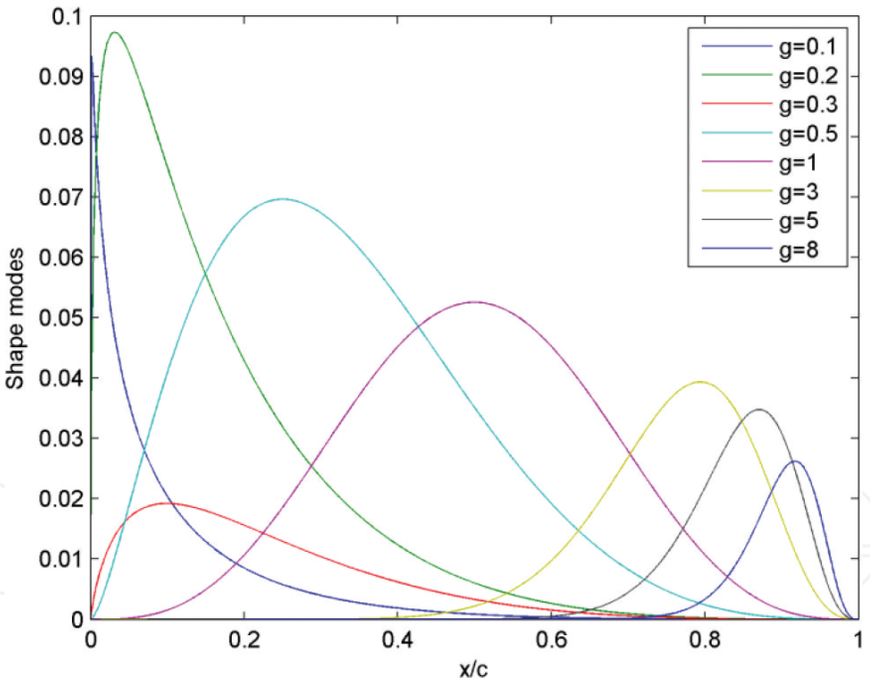

Figure 1. Example of the shape function.

Figure 1 shows an example of such shape perturbation function. It is possible to add more shape modes to put more focus at any chord-wise location. For example, adding more values around g = 0.1 leads to more detailed changes at the leading edge. The sum of the mode shapes will be added to the reference airfoil. At every iteration, the amplitude coefficients $f_{u,l}$ are updated until the final airfoil shape is found.

http://dx.doi.org/10.5772/63335

2.3. The objective

The design objective is the blending of power coefficient and rotor solidity such that

$$\text{Obj} = kC_p + (1-k)/\sigma \tag{6}$$

where k = 0.5 for airfoil section in the middle part of the blade. The k value shall be modified along the blade station while the solidity changes.

To obtain a good off-design property, the power coefficient is weighted between clean and rough conditions with the angle of attack ranging from α = 3° to α = 10°:

$$C_p = w\sum_{10}^{\alpha=3} C_p^{\text{clean}} + (1-w)\sum_{10}^{\alpha=3} C_p^{\text{rough}} \tag{7}$$

By using a weighting factor$w$ for the clean and rough conditions, Eq. (7) indicates that the resulted power coefficient will be less sensitive to surface roughness and will keep high value over a wide range of AOAs.

2.4. The constraints

From the aerodynamic point of view, the lift and the lift to drag ratio are already included in the C_p calculations, which are defined as the objective. The main constraint is set for the leading edge roughness sensitivity such that ΔC_l is constrained between the clean and rough cases. In other words, the performance between clean and rough airfoils should be as small as possible. Another important constraint to design a low-noise airfoil is the sound pressure level (SPL) such that SPL< N (dB). To estimate the noise generated from an airfoil, a 2D version of the semi-empirical model was developed, which was originally developed by Brook et al. [13] using acoustic measurements for a NACA 0012 airfoil and improved by using the actual boundary layer quantities of individual airfoils. For more details about the noise prediction model, the reader is referred to [13, 14].

2.5. Optimization results

In **Figure 2**, airfoils with a relative thickness of 18, 21 and 24% are shown for each airfoil family. The LN1xx airfoil shapes are designed with the Joukowski transformation. The LN2xx airfoils are generated with the shape perturbation method based on the LN1xx airfoils. And the LN3xx airfoils are further optimized for higher Reynolds number based on the LN2xx airfoils. The advantage is that there are less three-dimensional effects due to curvature change along the blade span; in other words, the airfoils are designed to have smooth geometrical transition between each other.

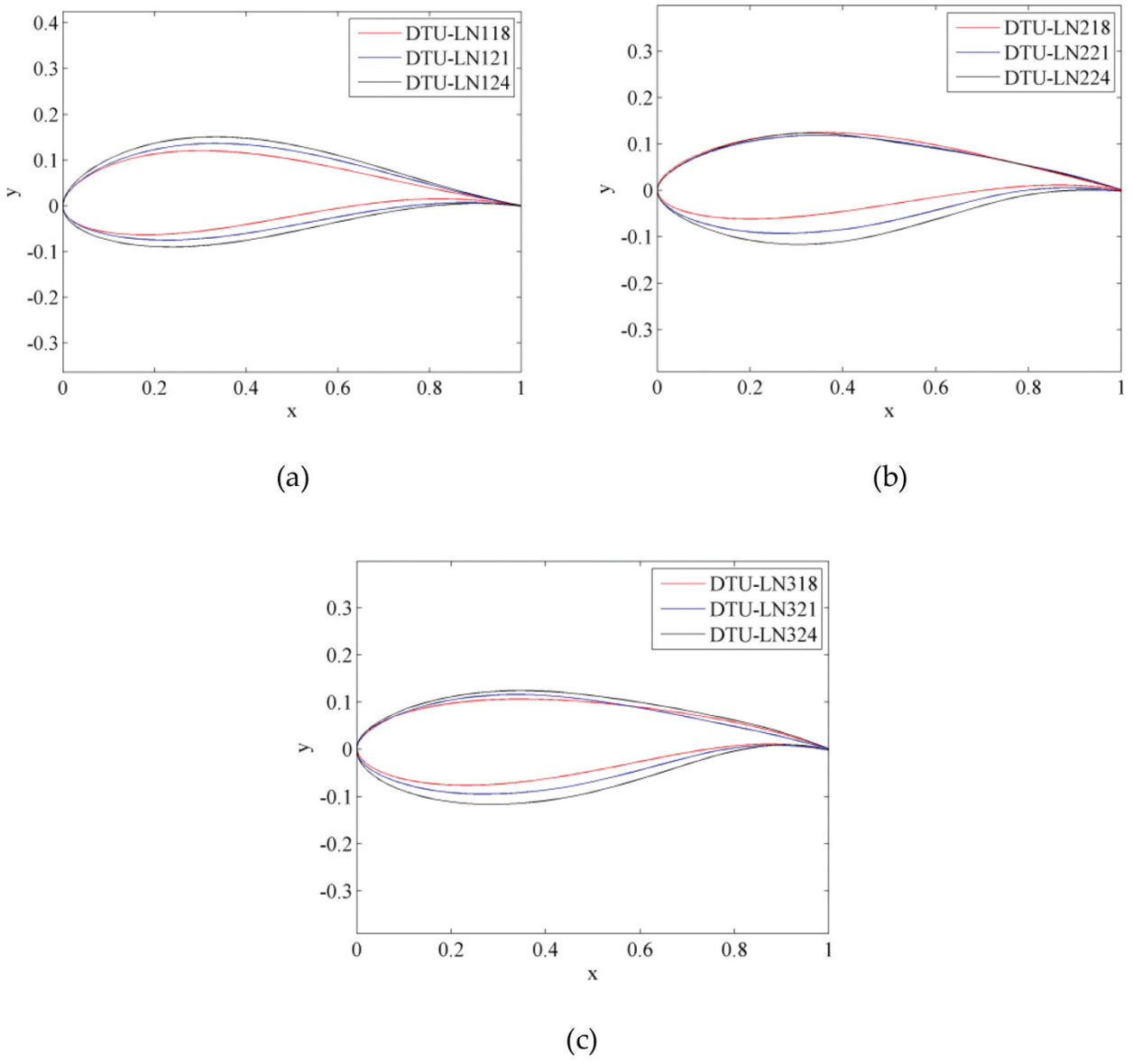

Figure 2. The airfoil families: (a) DTU-LN1xx; (b) DTU-LN2xx and (c) DTU-LN3xx.

3. The integrated design of airfoil and blade

The integrated design of airfoil family and blade can start from the BEM analysis of an airfoil section at a given blade station. The core of the analysis is the iterative computation of the power coefficient of a given airfoil during each step of optimization. The power performance has been used as a key reference number during design process [16], which is the most important measure of a rotor. With the aim of decreasing material cost, we introduce the rotor solidity as another parameter together with the power coefficient. In this analysis, we also involve the Prandtl's tip correction to the integrated design where the design of thin airfoils near the tip might be affected.

http://dx.doi.org/10.5772/63335

According to the 1D momentum theory, the solution of the power coefficient is maximized when the axial induction factor is $a = 1/3$, even though advanced computations show that the maximum power efficiency is obtained at slightly higher axial induction than $a = 1/3$. With this condition being valid, it can be shown that the power coefficient of an airfoil section can be written as

$$C_{\mathrm{p}} = \left[\left(1-a\right)^2 + x\left(1+a'\right)^2\right] xC_{\mathrm{t}}\sigma \tag{8}$$

with the solidity defined as

$$\sigma = 2F\sin^2\left(\phi\right)/C_{\mathrm{n}} \tag{9}$$

where a and a' are the axial- and tangential-induced velocity interference factors, respectively, x is the local speed ratio, C_{t} and C_{n} are the tangential and axial force coefficients, respectively, σ is the rotor solidity, ϕ is the local flow geometry and F denotes the Prandtl's tip loss function.

As is known that the Prandtl's tip loss function corrects the assumption of a disk, therefore to consider rotors with a finite number of blades, the correction has to be implemented to the blade design as well as the airfoil design. Different tip loss functions can be used for such design purposes [17]. A well-known tip correction model proposed by Prandtl reads

$$F = 2\cos^{-1}\left(e^{-f}\right)/\pi \tag{10}$$

Where

$$f = B\left(R-r\right)/\left(2r\sin\phi\right) \tag{11}$$

In Eq. (8), not all of the variables have been explicitly known. An assumption made for the axial induction factor is that $a = 1/3$. Other parameters can be separated into two groups. Parameters in group 1 are the values that will not enter into the BEM iterations, such as the local speed ratio x, the local length of the blade r, the total length of blade R, the number of blades B and the airfoil normal and tangential force coefficients. To compute the tangential force (C_{t}) and normal force (C_{n}), the lift and drag coefficients, c_{l} and c_{d} from the airfoil computations, are needed during every iteration of airfoil optimization, such that

$$C_t = c_{\mathrm{l}}\left(\sin\phi - c_{\mathrm{d}}/c_{\mathrm{l}}\cos\phi\right) \tag{12}$$

$$C_n = c_l\left(\cos\phi + c_d / c_l \sin\phi\right) \tag{13}$$

The other group of the variables will be iteratively solved due to their dependency. These parameters are the power coefficient C_p, the flow angle ϕ and the tangential induction factor a'. The values of C_p, ϕ and a' are initialized with zero before the first BEM iteration. After several iterations, the highest C_p for the present flow condition is obtained. The process of finding maximum C_p is repeated for both clean and rough surface conditions. For each clean and rough surface condition, the angles of attack to be considered are from 3° to 10°. The surface roughness weighted C_p over a wide range of angles of attack is used as one of the airfoil design objectives. These procedures are repeated for each airfoil generation until the optimum airfoil is found.

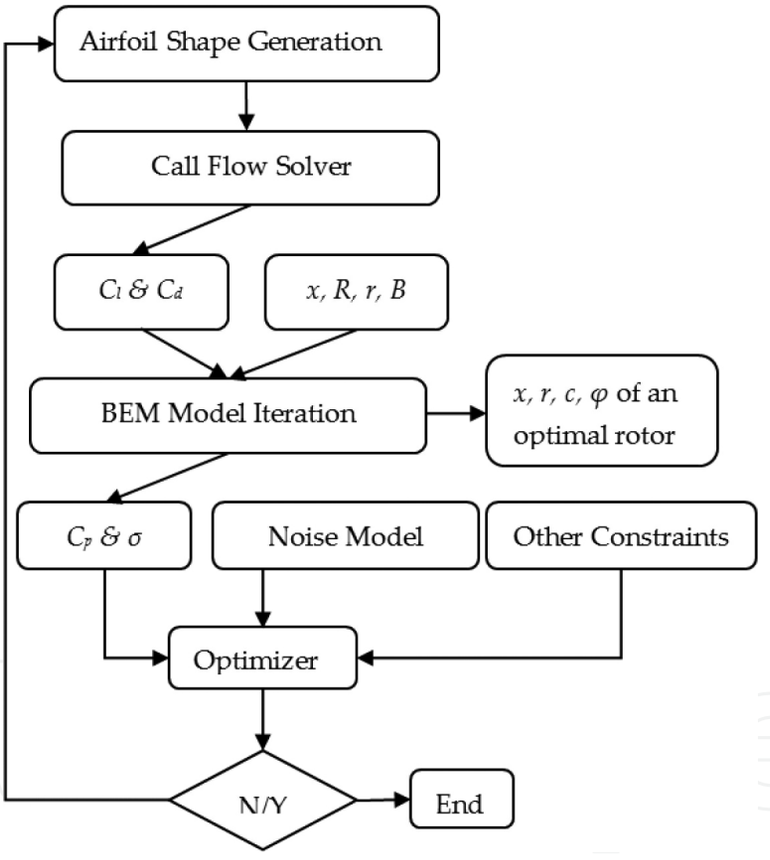

Figure 3. Flowchart of the integrated design method.

The integrated design process is summarized in **Figure 3**. As seen in the flowchart, the main loop goes through the airfoil shape optimization and the BEM iteration is inside the main loop. The BEM calculation is an important part of the integrated design concept that links the airfoil optimization with the optimal blade design. The BEM iteration requires input from airfoil aerodynamics, blade local speed ratio, etc. When the BEM converges, it writes an output to both the airfoil optimizer and results in a temporal optimal rotor (according to the temporally

http://dx.doi.org/10.5772/63335

obtained airfoil). The final optimal rotor is found when the airfoil optimizer finds a converged solution at each blade spanwise position.

4. Results and validations of airfoil and blade design

In this section, results are presented for both aerodynamics and aeroacoustics of airfoils and wind turbines. Several in-house developed models, Q^{3}UIC [18], EllipSys [19, 20] and BPM noise [14] programs, are used for design or cross comparisons.

4.1. Airfoil aerodynamics and noise

The pressure coefficient of the LN118 airfoil is simulated and compared with the wind tunnel measurements. With a wind speed of 60 m/s, the highest Reynolds number is achieved at about 2.1×10^6. In **Figure 4**, different models are compared with experiments. As seen from the comparisons, the three numerical methods, Xfoil, Q^{3}UIC and EllipSys can predict correctly C_p at angles of attack of 6.7°and 9.6°.

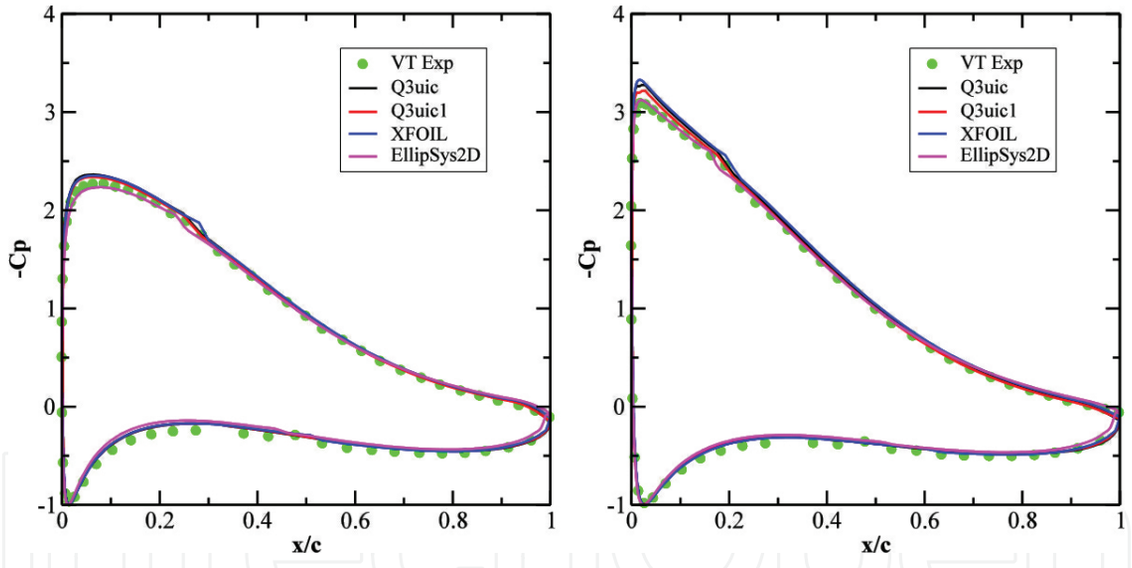

Figure 4. Comparisons of the surface pressure coefficient of a clean LN118 airfoil at $Re = 2.1 \times 10^6$ and angles of attack of 6.7°(left) and 9.6°(right).

As shown in **Figure 5**, the sound pressure level is calculated at a reference point of 1.62 m away from the trailing edge and at 90° direction. The noise levels are compared for flows past the LN118 and NACA 64618 airfoils at a wind speed of 30 m/s. At a same lift coefficient of 0.52 (**Figure 5(a)**), the experiments show that the LN118 airfoil produces lower noise level below the frequency of 3000 Hz. Similar results are observed at a lift coefficient of 0.95 (**Figure 5(b)**). The noise prediction model is also shown to be compared with the measurement. As shown in the figure, the predicted airfoil noise slightly overpredicts the noise emission from both airfoils but the relative differences between the noise levels are found to be similar from

computation and experiment. From the predictions, the main differences between the two airfoils are seen in the frequency region below 500 Hz.

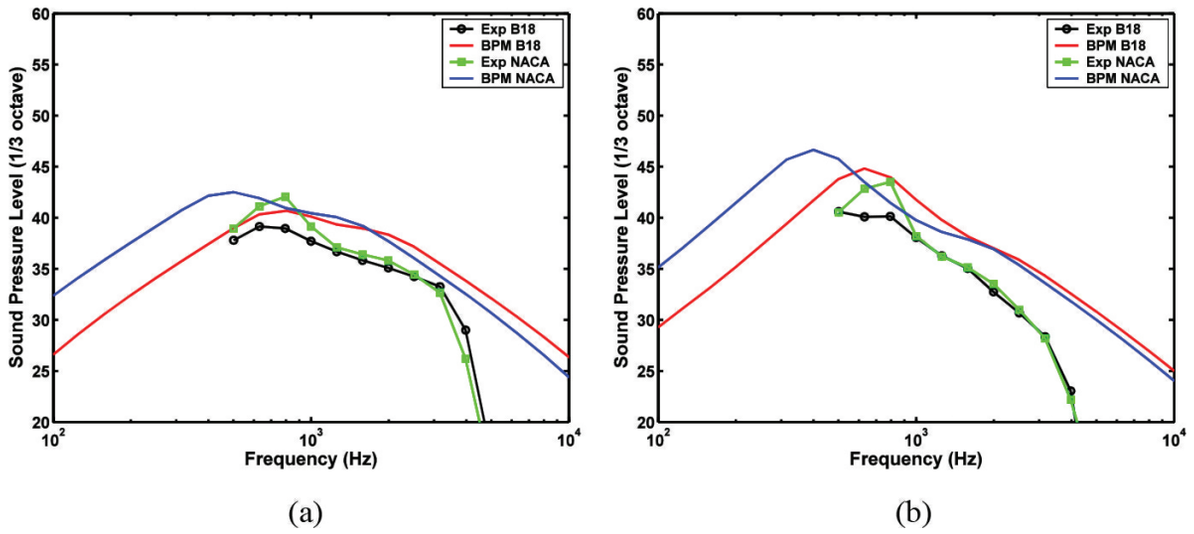

Figure 5. The measured and calculated 1/3-octave sound pressure level at a distance of 1.62 m and 90° direction from the LN118 airfoil and from the NACA 64618 airfoil at a wind speed of 30 m/s and $C_l = 0.52$ (a) and $C_l = 0.95$ (b).

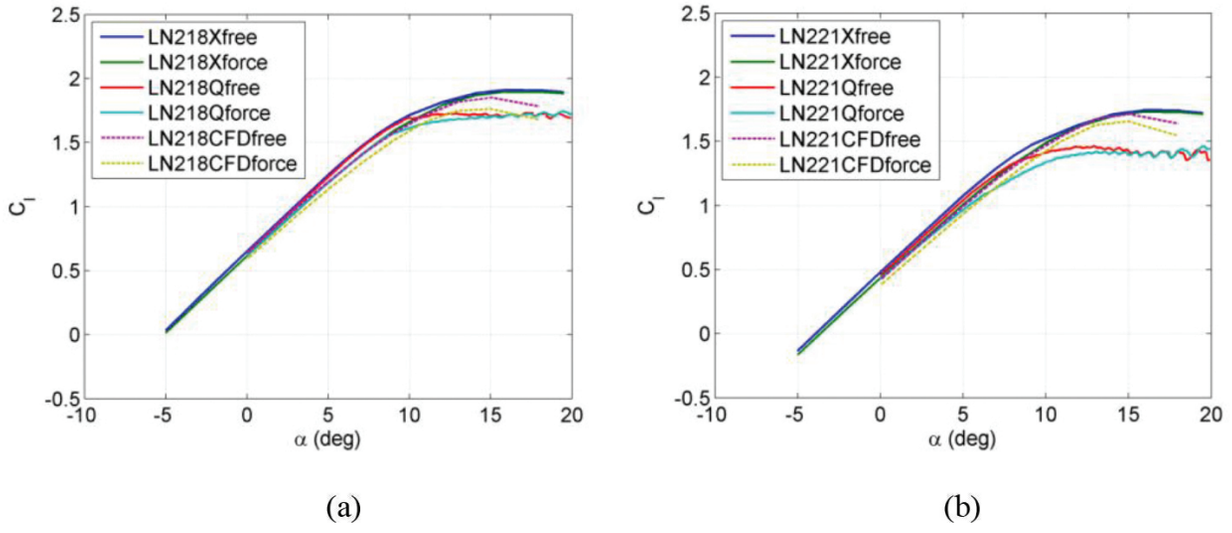

Figure 6. Comparisons of lift coefficient in free and force transition conditions using Xfoil, Q^{3}UIC and EllipSys.

To show surface roughness sensitivity, we compute the lift coefficient of the LN218 and LN221 airfoils up to stall angle of attack with free and force transition models. In **Figure 6**, results from the Xfoil (Xfree/force), Q^{3}UIC (Qfree/force) and EllipSys (CFDfree/force) are compared for the LN218 (**Figure 6(a)**) and LN221 (**Figure 6(b)**) airfoils. In the linear lift region, the results

http://dx.doi.org/10.5772/63335

are very similar. In the stall region, CFD (Computational Fluid Dynamics) results are in between Xfoil and Q^{3}UIC. It is important to see that the performance of the airfoils is very insensitive to the surface roughness.

4.2. Rotor aerodynamics and noise prediction

In this section, two of the newly designed in-house rotors are used for various simulations. The rotor sizes of the two wind turbines are 40 m and 130 m with the rated power of 3 MW and 20 MW, respectively. From the size of the two turbines, the design should have covered range of MW size wind turbines. The 3 MW wind turbine represents most of the existing commercial wind turbines. The design of the 20 MW wind turbine is more aimed at next 5–10-year development. To perform rotor simulations, the input of airfoil data to the BEM model is obtained from Xfoil calculations. By comparing the force distributions calculated from BEM (based on 2D airfoil data) and from CFD (based on full 3D flow), it is possible to identify the influence from the 2D design tools. **Figure 7** shows the platform of the 20 MW wind turbine blade; it is resulted from the iteration process as shown in **Figure 3**. An example of the full rotor CFD simulation for the 20 MW rotor is provided in **Figure 8**. This figure shows contour plots of the surface pressure coefficient and the individual pressure contours at the five designed blade sections, which represent the LN318, 21, 24, 27 and 30 airfoils.

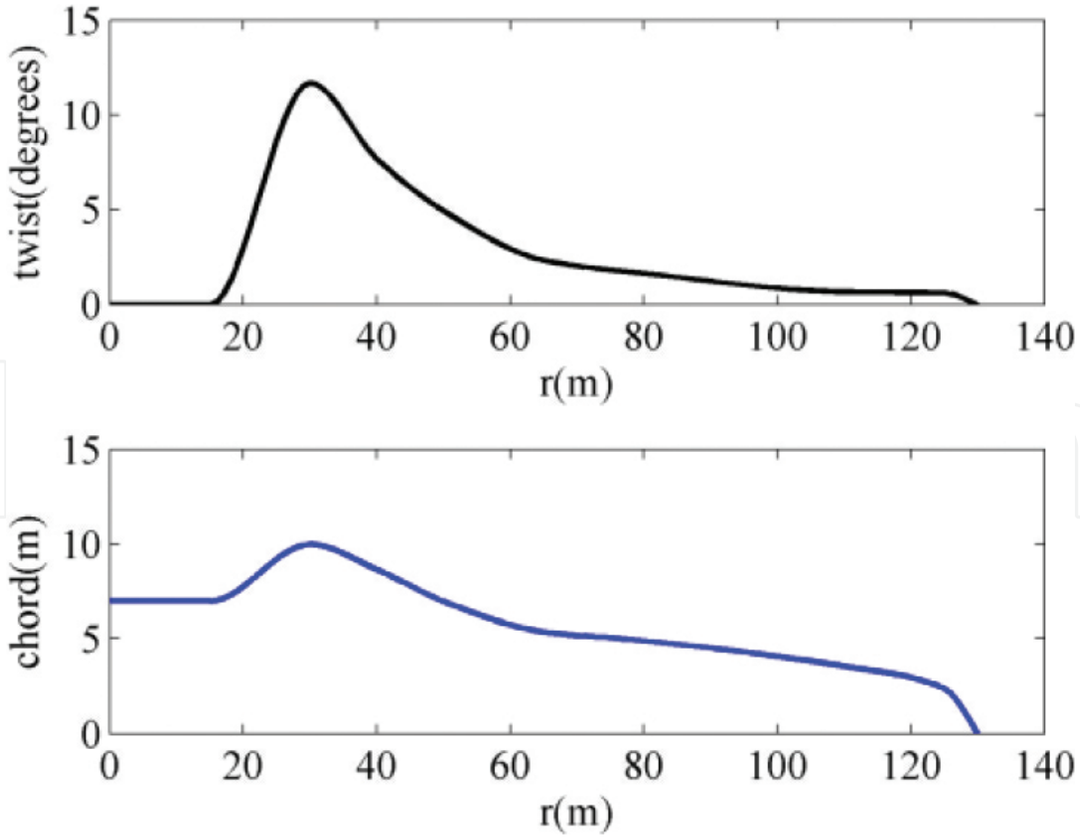

Figure 7. Plot blade twist and chord for 20 MW (airfoil family 2).

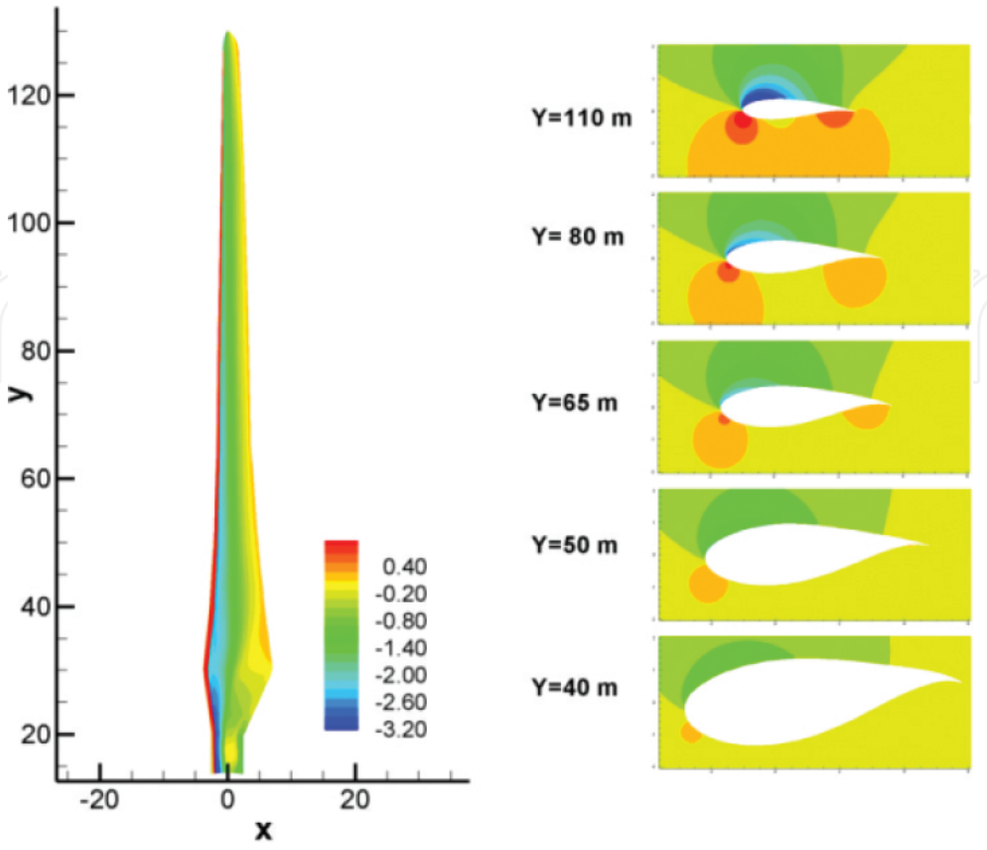

Figure 8. Contour plot of the surface pressure coefficient and pressure contour at five blade sections.

Since these airfoils are designed by integrating Xfoil and BEM methods, it will be interesting to compare pressure forces along each blade section using Xfoil and CFD. The pressure distribution at a blade section can be obtained after post-processing from the CFD calculation, for example, extracting the surface pressure from **Figure 8**. Since the BEM calculations already provide angles of attack along the blade, angles of attack are known for each blade spanwise location. Using these angles of attack to perform Xfoil simulation with a free transition model, the pressure coefficients are known from Xfoil. With the same free transition model and the same n-factor, the surface pressure obtained from Xfoil and CFD are compared at blade positions of Y = 80 m and Y = 40 m for the 20 MW rotor case. **Figure 10** reflects a few facts: (1) The BEM model performs very well, which provides accurate flow condition; (2) Xfoil is in well agreement with CFD prediction at the blade outer part; (3) Overprediction from the Xfoil code becomes evident at blade inboard part.

In **Figure 9**, the results from BEM and CFD are compared. It is noticed that the blade normal force (F_n) and the tangential force (F_t) obtained from CFD and BEM are close with each other, both for the 20 MW turbine (**Figure 9(a)**) and the 3 MW turbine (**Figure 9(b)**), respectively. It is found that CFD predicts slightly higher forces than BEM which is mostly observed from 40 m < r < 130 m (**Figure 9(a)**) and 15 m < r < 35 m (**Figure 9(b)**). Such kind of difference is often related to the rotational effect that has been modelled by CFD but not enough counted by BEM. The laminar boundary layer tends to be smaller while rotation is taking into effect, this leads

http://dx.doi.org/10.5772/63335

to a higher force in reality. For more accurate aerodynamic load prediction, the airfoil data should be corrected for rotational effect before applying to a BEM model. Overprediction of forces for thick airfoils and/or high angles of attack indicates the limitation of the Xfoil code. Although CFD simulation is much more accurate in most cases, it has not reached the stage so that it can be directly used as a design tool. Also, to better design or predict forces at blade inboard part, it is necessary to use some more sophisticated methods to remedy the existing engineering tools.

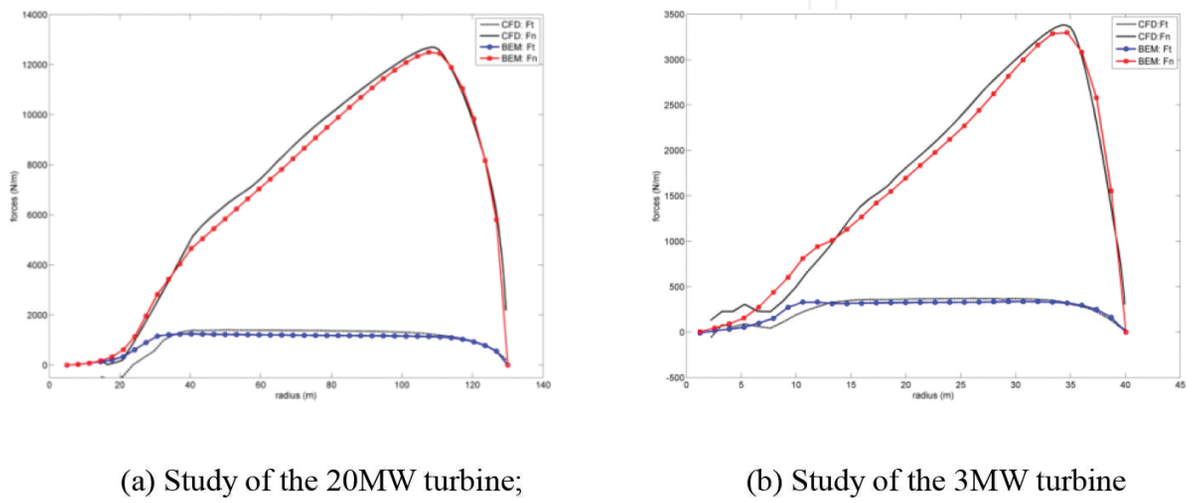

Figure 9. Simulated forces along blade for: (a) the 20 MW and (b) the 3 MW wind turbine at wind speed of 10 m/s.

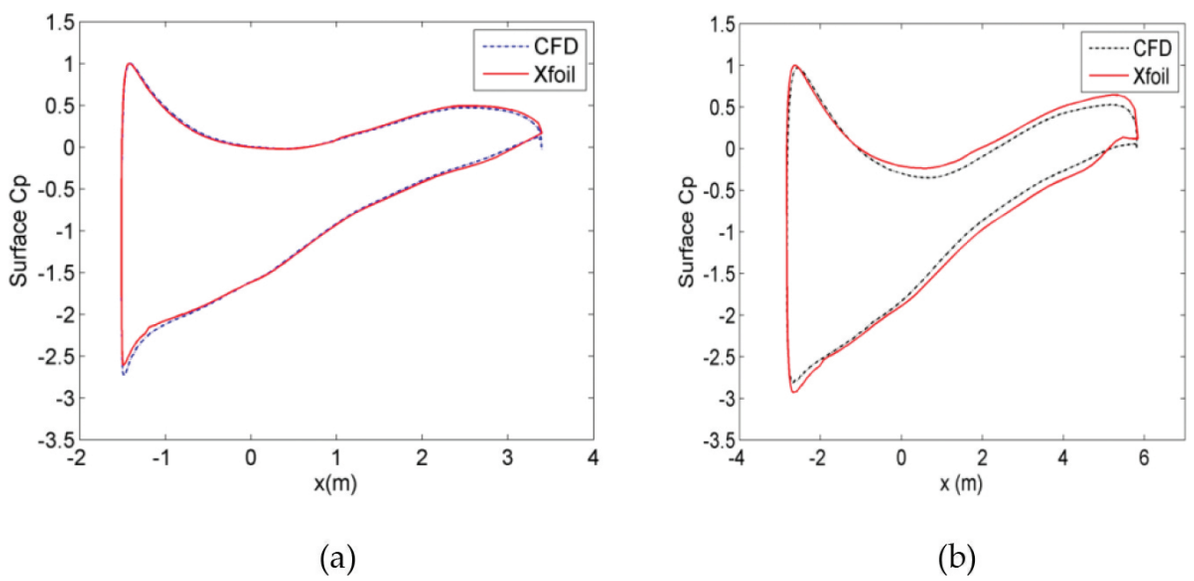

Figure 10. Surface pressure coefficients computed from CFD and Xfoil at $Y = 80$ m (a) and $Y = 40$ m (b).

The noise simulation for the two wind turbines is shown in **Figure 11**. The overall A-weighted sound pressure levels from the 20 MW wind turbine are 47.5 and 42.9 dBA for the 3 MW wind turbine. The individual noise mechanisms are similar, except that the 20 MW wind turbine has a lower peak frequency than the 3 MW wind turbine.

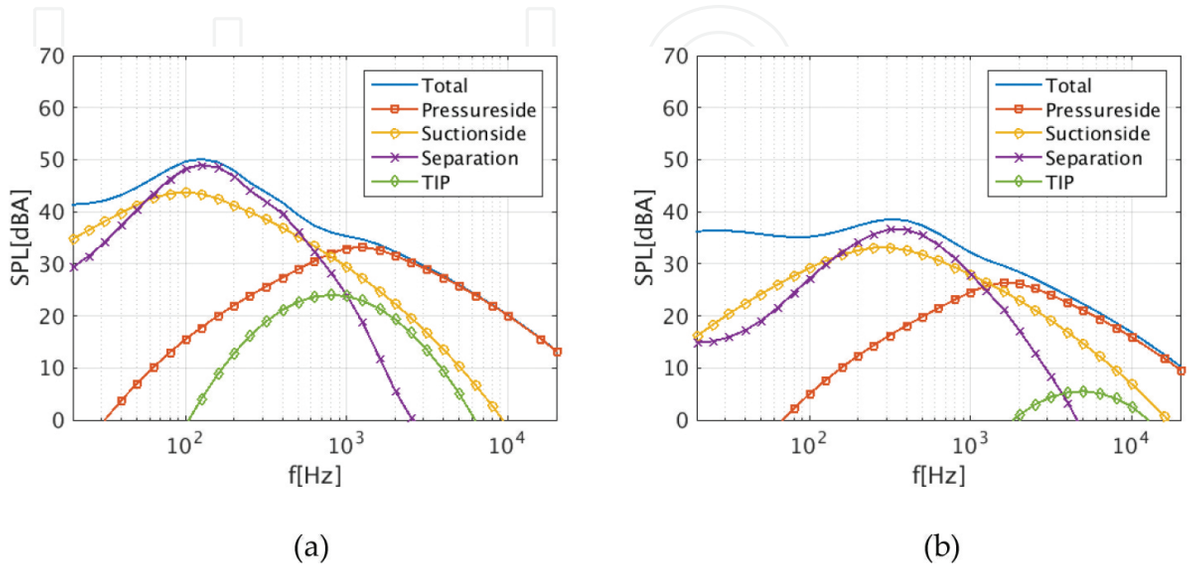

Figure 11. Wind turbine noise simulations: (a) 20 MW turbine (47.5 dBA) and (b) 3 MW turbine (42.9 dBA), measured at 200 m downstream at ground height of 2 m.

4.3. Further reduction of trailing edge noise

Even after the design of a low-noise blade, it is possible to further reduce noise from the trailing edge. This section briefly introduces the trailing edge serration as the additional add at the trailing edge. Several methods already exist for airfoil trailing noise simulation; however, models such as BPM and TNO [21] cannot be directly used for modelling noise with serrations. Based on the assumption of a flat plate, Howe [22] derived a noise prediction model for a saw-tooth trailing edge at zero angle of attack. In the model, the far-field noise spectrum is related to the aerodynamic pressure spectrum. However, theoretical prediction using Howe's theory does not fit well with some of the airfoil noise measurements in terms of overall noise magnitude. It is expected that advanced computational aeroacoustic (CAA) methods provide more accurate prediction of noise from a serrated trailing edge. In this study, the acoustic simulation method is the integrated representation of Ffowcs Williams-Hawkings (FW-H) acoustic analogy, more information related to the methods are referred in references [23, 24]. The acoustic solver is implemented in the in-house flow solver EllipSys3D. The unsteady turbulent flow over airfoil is solved by the large eddy simulation (LES) approach. The airfoil to be investigated is the LN118 airfoil. The surface mesh and the side view of the volume mesh are shown in **Figure 12**. The baseline LN118 airfoil is attached with serrations at the trailing edge.

http://dx.doi.org/10.5772/63335

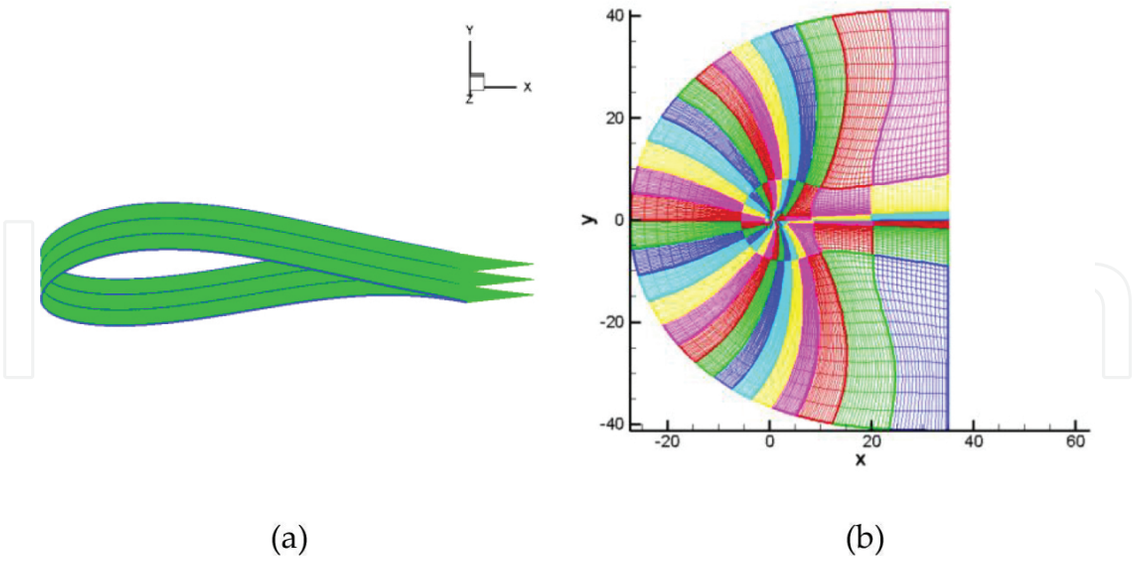

Figure 12. Mesh of the wall surfaces (a) and side view of mesh (b).

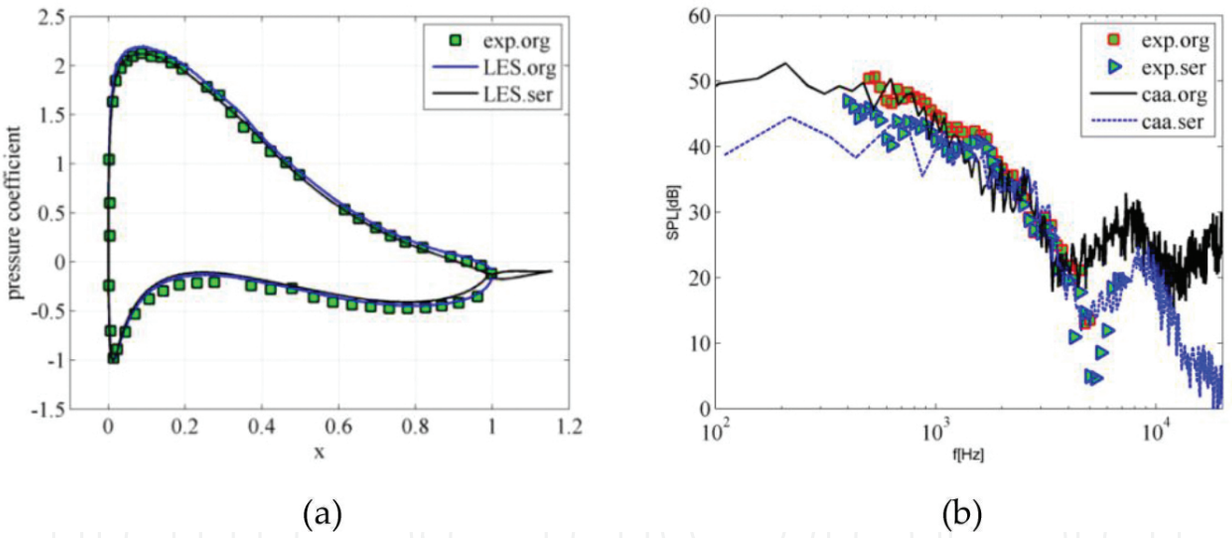

Figure 13. Comparisons of surface pressure (a) and noise spectra (b) against measurements at an angle of attack of 6°.

The wind speed used for the simulation is 45 m/s, the airfoil chord is 0.6 m, the serration length is 16.7% of the baseline airfoil chord and the wave number is 50% of the serration length. The surface pressure at angle of attack 6° is extracted from LES result. In **Figure 13**, the flow results from LES are first compared with the wind tunnel experiment. The results show very small difference with experiment either for the original LN118 airfoil or for the airfoil with serration. Only small difference is observed near the trailing edge. The results indicate that the serration does not provide a big influence on the airfoil aerodynamics. On the right side of **Figure 13**, the measured and simulated noise spectra are compared, which show some good agreement. The general trend from both results confirms the effect of the trailing edge serration.

5. Conclusion

In this chapter, the design of several airfoil families and wind turbine blades are introduced. Different aerodynamic and aeroacoustic tools are involved into the design and validation of the low-noise airfoil/blade design. The overall aerodynamic performance is good for all the airfoils. The noise emission is controlled by the optimization process. Large MW size wind turbine blade can be designed with integrated method where the power coefficient is significantly large while the noise level is restricted at low level. The noise spectrum is computed with semi-empirical model and CAA methods. The power and force are computed both by blade element momentum method and CFD with body-fitted mesh. Comparisons with measurements and other cross validations show that low-noise blade can be achieved, which still maintains high aerodynamic performance.

Author details

Wei Jun Zhu*, Wen Zhong Shen and Jens Nørkær Sørensen

*Address all correspondence to: wjzh@dtu.dk

Department of Wind Energy, Technical University of Denmark, Lyngby, Denmark

School of Hydraulic, Energy and Power Engineering, Yangzhou University, Yangzhou, China

References

[1] Bo Søndergaard. Noise and low frequency noise from wind turbines. In: Inter.noise 2014. Melbourne, Australia; November 2014. pp. 1–12.

[2] Thiele HM. Growian rotor blades: production development, construction and test. Report Number: NASA TM-77479; Publication data: Jul 01,1984.

[3] Tangler JL, Somers DM. Status of the special purpose airfoil families. In: Proceedings of WINDPOWER'87, San Francisco; 1987. pp. 3264.

[4] Tangler JL, Somers DM. NREL airfoil families for HAWT's. In: Proceedings of WINDPOWER'95, Washington, D.C.; 1995. pp. 117–123.

[5] Björk A. Airfoil design for variable rpm horizontal axis wind turbines. In: Proceedings of EWEC'89, Glasgow, Scotland; 1989.

[6] Björk A. Coordinates and calculations for the FFA-W1-xxx, FFA-W2-xxx and FFA-w3-xxx series of airfoils for horizontal axis wind turbines, Sweden, Stockholm; 1990.

[7] Timmer WA, Van Rooij R. Summary of the Delft university wind turbine dedicated airfoils. Journal of Solar Energy Engineering. 2003;125:488–496.

[8] Dahl KS, Fuglsang P. Design of the wind turbine airfoil family RISØ-A-XX. RISØ National Laboratory; Roskilde, Denmark; 1998 [RISØ-R-1024].

[9] Fuglsang P, Bak C. Development of the RISØ wind turbine airfoils. Wind Energy. 2004;7:145–162.

[10] Wang XD, Chen J, Shen WZ, Zhu WJ, Sørensen JN. Airfoils and methods for designing airfoils [P]. Application No. PCT/EP2010/056810, International patent application.

[11] Wang XD, Chen J, Shen WZ, Zhang S. Integration study on airfoil profile for wind turbines. Journal of China Mechanical Engineering. 2009;20(2):211–228.

[12] Chen JT, Zhu WJ, Fischer A, García NR, Madsen J, Chen J, Shen WZ. Design and validation of the high performance and low noise Chong Qing University and Technical University of Denmark LN1 airfoils. Wind Energy. 2014;17(12):1817–1833. DOI: 10.1002/we.1668.

[13] Brooks TF, Pope DS, Marcolini MA. Airfoil self-noise and prediction. Reference Publication 1218, National Aeronautics and Space Administration, USA; 1989.

[14] Zhu WJ, Heilskov N, Shen WZ, Sørensen JN. Modeling of aerodynamically generated noise from wind turbines. Journal of Solar Energy Engineering. 2005;127:517–528.

[15] Drela M. XFOIL: an analysis and design system for low Reynolds number airfoils. In: Conference on low Reynolds number aerodynamics, University of Notre Dame; 1989.

[16] Bak C. Research in aeroelasticity EFP-2006: key parameters in aerodynamic rotor design. RISØ National Laboratory, Roskilde, Denmark; 2007 [RISØ-R-1611(EN)].

[17] Shen WZ, Mikkelsen R, Sørensen JN. Tip loss corrections for wind turbine computations. Wind Energy. 2005;(8):457–475.

[18] Ramos García N, Sørensen JN, Shen WZ. A strong viscous–inviscid interaction model for rotating airfoils. Wind Energy. 2014;17(12):1957–1984. DOI: 10.1002/we.1677.

[19] Michelsen JA. Basis3D – a platform for development of multiblock PDE solvers. Technical Report AFM, Technical University of Denmark; Denmark: 1992.

[20] Sørensen NN. General purpose flow solver applied over hills. RISØ National Laboratory, Roskilde, Denmark; 1995 [RISØ-R-827(EN)].

[21] Parchen R. Progress report DRAW: a prediction scheme for trailing-edge noise based on detailed boundary-layer characteristics. TNO Rept. HAGRPT-980023 TNO Institute of Applied Physics, The Netherlands; 1998.

[22] Howe MS. Noise produced by a sawtooth trailing edge. Journal of the Acoustic Society of America. 1991;90(1):482–487.

[23] Ffowcs Williams JE, Hawkings DL. Sound generated by turbulence and surfaces in arbitrary motion. Philosophical Transactions of the Royal Society. 1969;264:321–342.

[24] Farassat F. Derivation of formulations 1 and 1A of Farassat. NASA/TM-2007-214853; 2007. http://ntrs.nasa.gov/archive/nasa/casi.ntrs.nasa.gov/20070010579.pdf

IntechOpen